PLOS GENETICS

RESEARCH ARTICLE

A defining member of the new cysteine-cradle family is an aECM protein signalling skin damage in *C. elegans*

Thomas Sonntag[1], Shizue Omi[1], Antonina Andreeva[2], Claire Valotteau[3], Jeanne Eichelbrenner[1], Andrew D. Chisholm[4], Jordan D. Ward[5], Nathalie Pujol[1]*

1 Aix Marseille Univ, INSERM, CNRS, CIML, Turing Centre for Living Systems, Marseille, France, **2** European Molecular Biology Laboratory, European Bioinformatics Institute (EMBL-EBI), Wellcome Genome Campus, Hinxton, Cambridgeshire, United Kingdom, **3** Aix-Marseille Univ, INSERM, DyNaMo, Turing Centre for Living Systems, Marseille, France, **4** Department of Cell and Developmental Biology, School of Biological Sciences, University of California San Diego, La Jolla, California, United States of America, **5** Department of Molecular, Cell, and Developmental Biology, University of California Santa Cruz, Santa Cruz, California, United States of America

* pujol@ciml.univ-mrs.fr

OPEN ACCESS

Citation: Sonntag T, Omi S, Andreeva A, Valotteau C, Eichelbrenner J, Chisholm AD, et al. (2025) A defining member of the new cysteine-cradle family is an aECM protein signalling skin damage in C. elegans. PLoS Genet 21(3): e1011593. https://doi.org/10.1371/journal.pgen.1011593

Editor: Fengwei Yu, National University of Singapore, SINGAPORE

Received: November 6, 2024

Accepted: January 27, 2025

Published: March 20, 2025

Data availability statement: All relevant data are within the manuscript and its Supporting Information files, The novel domain has been deposited as a new entry in Pfam is available since the release 37.1 (https://www.ebi.ac.uk/interpro/entry/pfam/PF23626/).

Funding: The project leading to this publication has received funding from France 2030, the

Abstract

Apical extracellular matrices (aECMs) act as crucial barriers, and communicate with the epidermis to trigger protective responses following injury or infection. In *Caenorhabditis elegans*, the skin aECM, the cuticle, is produced by the epidermis and is decorated with periodic circumferential furrows. We previously showed that mutants lacking cuticle furrows exhibit persistent immune activation (PIA), providing a valuable model to study the link between cuticle damage and immune response. In a genetic suppressor screen, we identified *spia-1* as a key gene downstream of furrow collagens and upstream of immune signalling. *spia-1* expression oscillates during larval development, peaking between each moult together with patterning cuticular components. It encodes a secreted protein that localises to furrows. SPIA-1 shares a novel cysteine-cradle domain with other aECM proteins. SPIA-1 mediates immune activation in response to furrow loss and is proposed to act as an extracellular signal activator of cuticle damage. This research provides a molecular insight into intricate interplay between cuticle integrity and epidermal immune activation in *C. elegans*.

Author summary

This study uncovers the role of SPIA-1, a newly discovered protein in the roundworm *Caenorhabditis elegans*, in detecting damage to its outer protective layer, the cuticle. SPIA-1 is found in furrows of the cuticle, but when these furrows are absent—a condition linked to constant immune activation—SPIA-1's normal positioning is disrupted. Removing SPIA-1 in these mutants reduces immune activation, showing that SPIA-1 plays a critical role in signalling damage and triggering immune responses. SPIA-1 is unique to nematodes and contains a novel structural domain, which was named the "cysteine-cradle domain" due to its distinctive shape. This domain is also found in five other poorly

French Government program managed by the French National Research Agency (ANR-16-CONV-0001) and from Excellence Initiative of Aix-Marseille University - A*MIDEX. Also supported by the French National Research Agency ANR-22-CE13-0037-01 to NP, from ATIP Avenir and ITMO Cancer of Aviesan on funds Cancer 2021 to CV, from institutional grants from CNRS to CV and NP and Aix Marseille University to JE, from the Biotechnology and Biological Sciences Research Council and the NSF Directorate for Biological Sciences (BB/X012492/1) to AA, and the National Institutes of Health to ADC (NIH R35GM134970) and JDW and ADC (NIH R21OD033663). The funders had no role in study design, data collection and analysis, decision to publish, or preparation of the manuscript. The funders had no role in study design, data collection and analysis, decision to publish, or preparation of the manuscript.

Competing interests: The authors have declared that no competing interests exist.

studied nematode proteins. The study not only sheds light on how *C. elegans* maintains its protective barrier and defends against damage but also sparks interest in a newly identified protein family.

Introduction

All multicellular organisms must protect themselves from injury and pathogens. *Caenorhabditis elegans* lacks an adaptive immune system and motile immune cells. Instead, it relies on its epithelial barriers to defend itself against environmental threats. This makes it a powerful model to address the question of how epithelial cells detect damage. In *C. elegans*, the skin is characterised by a rigid but flexible apical extracellular matrix (aECM), known as the cuticle, that surrounds a single syncytial epidermal layer (reviewed in [1]. The cuticle surface contains circumferential-oriented furrows distributed periodically over the entire body length [2–4]. Embryos assemble the first larval cuticle, and then during each larval stage, a new cuticle is assembled, and the old one shed, in a process known as moulting [5]. A transient precuticle is assembled to help to pattern the new cuticle and to shed the old one [1].

The cuticle serves not only as a protective barrier against environmental insults but also as a dynamic interface that communicates crucial signals to the underlying epidermal tissue. We have previously described how cuticle damage triggers a series of responses in the epidermis. These responses can be set off by physical injury, infection with the fungus *Drechmeria coniospora*, or during the cyclic process of moulting. The organism's ability to mount a protective transcriptional response maintains tissue integrity to combat potential threats [1,6,7].

Mutants lacking periodic furrows have emerged as a valuable model for studying the interplay between cuticle integrity and epidermal immune activation. Mutations in any of the six furrow collagens (DPY-2, DPY-3, DPY-7, DPY-8, DPY-9, DPY-10) lead to the absence of periodic furrows in the cuticle [4,8,9]. We have previously shown that the same mutations exhibit a persistent immune activation (PIA), similar to the response triggered by moulting, physical injury or skin infection [10–14]. This immune response involves the activation of the p38 MAPK/PMK-1 signalling pathway and the downstream SNF-12/SLC6 transporter and STAT-like transcription factor STA-2 [11–13]. During infection or injury, the most upstream components known are the Damage Associated Molecular Pattern (DAMP) receptor DCAR-1, a GPCR, and the Gα protein GPA-12 [14]. While loss of STA-2 or SNF-12 fully abrogates the induction of an immune response in furrow collagen mutants, inactivation of DCAR-1 only reduces it partially [14]. We therefore proposed that a parallel mechanism must link the monitoring of furrow collagens' integrity to the activation of the immune response in the epidermis.

To gain deeper insights into how cuticle damage is sensed by the epidermis, we conducted a targeted genetic suppressor screen to identify genes acting downstream of furrow collagens and upstream of, or in parallel to, GPA-12. Notably, one suppressor identified in this screen harbours a mutation in the gene *spia-1* (*Suppressor of Persistent Immune Activation*). This gene encodes a small nematode-specific secreted protein sharing a C-terminal domain with five other *C. elegans* proteins, including DPY-6, a mucin-type protein with a conserved role in cuticle deposition [15]. The structured core of this common C-terminal domain (named CCD-aECM) is predicted to be formed by conserved cysteine interactions to allow potential homomeric and heteromeric interactions. Our expression and genetic analyses suggest that SPIA-1 functions as a secreted aECM protein, localised to the furrows, potentially relaying information about the state of the furrow collagens to the underlying epidermis.

Results & discussion

Identification of *spia-1* as a suppressor of a constitutive immune response

We previously showed that wounding and infection of *C. elegans* trigger an immune response, characterised by the induction of the expression of the antimicrobial peptide (AMP) gene *nlp-29* in the epidermis [6,7,14,16,17]. Interestingly, mutants in furrow collagens, which lack the organised circumferential furrow structure ("furrow-less mutants") [10], also have a persistent immune activation (PIA) [13,14,18], in parallel to constitutively active detoxification and hyperosmotic responses [12]. The fact that these 3 responses are induced by the absence of furrows, yet differ in their signalling and effectors, led to the suggestion that a cuticle-associated damage sensor coordinates these 3 responses [12].

To characterise this potential damage sensing mechanism, we conducted a genetic suppressor screen, designed to identify the upstream components of the pathway leading to the induction of the immune response in furrow-less mutants. The screen relies on the observation that a constitutively active form of GPA-12 (GPA-12gf) provokes a PIA by activating the p38/PMK-1 – STA-2 pathway, and on the use of a conditional promoter that is only active in the adult epidermis [19]. In addition to a construct expressing GPA-12gf uniquely in the adult epidermis, the strain IG1389 we designed has the well-characterised *frIs7* transgene containing the *nlp-29* promoter driving GFP expression (*nlp-29*p::GFP) and a control DsRed transgene constitutively expressed in the epidermis, providing an internal control for the integrity of the epidermis and nonspecific transgene silencing [7]. In the IG1389 strain, the *nlp-29*p::GFP reporter is not expressed in larvae but constitutively expressed in the adult, due to the expression of GPA-12gf ([20]; Fig 1A). When any of the six furrow collagen genes, including *dpy-7*, is inactivated by RNAi in this strain, worms exhibit a high level of GFP at all developmental stages (green larvae-green adults) (Figs 1A, 1B and S1A). In these conditions, inactivating any gene acting downstream of GPA-12, like *sta-2*, completely abolishes the expression of *nlp-29*p::GFP at all stages (red larvae-red adults; the so-called "no induction of peptide after infection" (Nipi) phenotype [7]) (Figs 1B and S1A). However, if the inactivated gene acts upstream of, or in parallel to, GPA-12, the expression of *nlp-29*p::GFP should be suppressed in larvae but reactivated by GPA-12gf in the adult (S1A Fig), as observed with *dcar-1,* which acts upstream of *gpa-12* (Fig 1B).

We mutagenised the strain IG1389 using ethyl methanesulfonate (EMS), then transferred synchronised F2 progeny onto *dpy-7* RNAi plates at the L1 stage and screened for mutants that suppressed the PIA phenotype. Many mutants corresponded to genes acting downstream of *gpa-12*, as they blocked the PIA at both larval and adult stages. Complementation tests allowed us to identify new alleles of components of the known pathway, including *snf-12(fr189)*. Interestingly, another subset of mutants had a phenotype comparable to *dcar-1*, i.e., the expression of *nlp-29*p::GFP was suppressed in larvae but reactivated in the adult. Among them, the *fr179* mutant had the clearest phenotype (Fig 1B). We called the *fr179* mutant *spia-1* (*Suppressor of Persistent Immune Activation).* We confirmed that in the absence of *dpy-7* RNAi, *spia-1(fr179)* mutation also did not suppress the *gpa-12*-induced PIA observed in adults, while *sta-2(ok1860)* completely abrogated it (S1B Fig). This data suggested that *spia-1* does not act downstream of *gpa-12*. Moreover, unlike *dcar-1* mutation, *spia-1(fr179)* partly blocked the PIA in adults, when it is provoked by a combination of *dpy-7* inactivation and GPA-12gf (Fig 1B), which means that the activation of GPA-12gf only partially restore *spia-1* suppression. Together, these data suggest that SPIA-1 acts in a non-redundant pathway parallel to DCAR-1/GPA-12.

We backcrossed the *spia-1(fr179)* strain relying on the suppression of *nlp-29*p::GFP induction upon *dpy-7* RNAi for the selection of *spia-1(fr179)* progeny. The underlying molecular

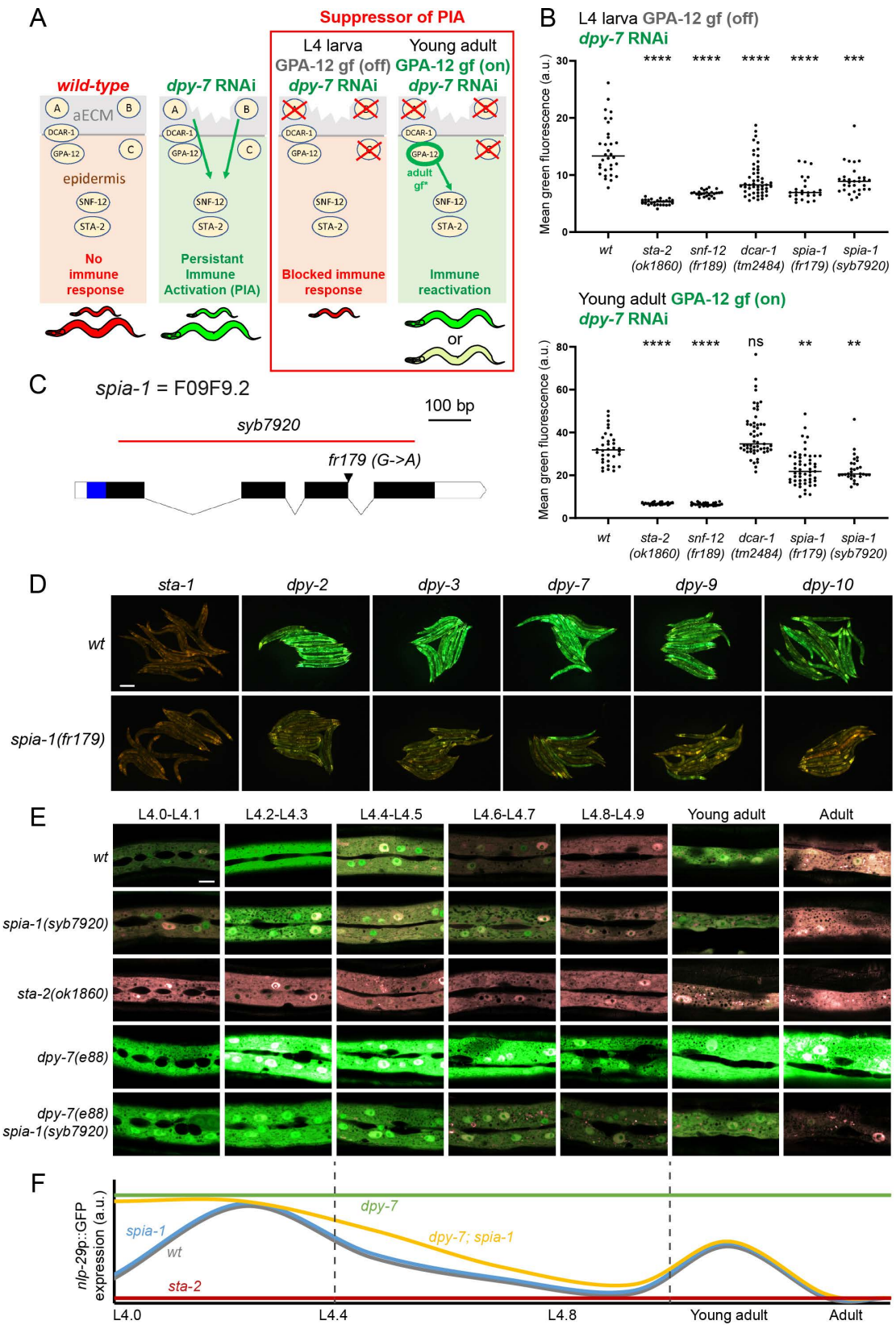

Fig 1. Loss of *spia-1* suppresses furrow collagen AMP induction. (A) Design of the suppressor screen. The strain carries the *frIs7* transgene, containing an AMP transcriptional reporter (*nlp-29*p::GFP) and a control transgene (*col-12*p::DsRed)

constitutively expressed in the epidermis. Under standard growth conditions, worms only express the control transgene and are red at all stages (left). RNAi inactivation of any furrow collagen gene, like *dpy-7*, leads to the expression of *nlp-29*p::GFP in a PMK-1/STA-2 dependent manner: worms appear "green" at all stages (middle). The strain used for the suppressor screen additionally bears the *frIs30* construct to express a gain of function of GPA-12 in the epidermis, only from the young adult stage (*col-19*p::GPA-12gf). In this strain, inactivation of a gene downstream of GPA-12 eliminates the expression of *nlp-29*p::GFP in both larvae and adults (Nipi phenotype [7]), whereas inactivation of any gene acting upstream of, or in parallel to, GPA-12, inhibits the expression of *nlp-29*p::GFP in the larvae but not in the adult due to the activation of GPA-12 (red larvae, green adults, right). This rescue is total if the targeted gene acts upstream of GPA-12 (A, *dcar-1*), but only partial if it acts in parallel to GPA-12 (B/C). (B) Quantification of the green fluorescence in worms carrying *frIs7* and *frIs30* constructs in different mutant backgrounds, upon *dpy-7* RNAi, in L4 and young adult stages (n>25). Statistics were made by comparing to the corresponding *wt* control; $^{**}p < 0.01$; $^{***}p < 0.001$; $^{****}p < 0.0001$. (C) Structure of the *spia-1* genomic locus. The location of the *fr179* mutation is indicated with an arrowhead, the extent of the *syb7920* deletion is shown with a red line. Exons are shown as black boxes, introns as solid lines. UTR are represented as white boxes; the blue region shows the sequence encoding the signal peptide of *spia-1*. (D) *spia-1(fr179)* suppresses the induction of *nlp-29*p::GFP in young adult worms after RNAi inactivation of furrow collagen genes. Wild-type and *spia-1(fr179)* mutants carrying the *frIs7* transgene were treated with the indicated RNAi bacteria, with *sta-1* used as a control (see Mat&Methods). Red and green fluorescences were visualised simultaneously in all images. Representative images of young adults from one of three experiments are shown; scale bar, 200 μm; see S1C and S1D Fig for quantification with the COPAS Biosort. (E) Oscillation of *nlp-29*p::GFP expression from L4 to adulthood. Representative confocal images of different mutant strains carrying the *frIs7* transgene, red and green fluorescences were visualised simultaneously. The L4 stage is subdivided into sub-stages with the shape of the vulva [23]; n>5, scale bar, 10 μm. (F) Proposed schematic illustration of *nlp-29*p::GFP oscillation shown in E. Expression levels are estimated and not to scale.

https://doi.org/10.1371/journal.pgen.1011593.g001

lesion was characterised by mapping through whole genome sequencing (WGS) of a pool of backcrossed *spia-1(fr179)* independent recombinant mutants [21,22]. The *spia-1(fr179)* worms carry a mutation in a splice donor site of the gene *F09F9.2* (hereafter *spia-1*), predicted to result in a transcript with a frameshift and the introduction of a premature stop codon leading to a truncated protein of 133 aa (Fig 1C). We generated by CRISPR the allele *spia-1(syb7920)*, bearing a deletion of 710 bp in *spia-1* with a modification of bp 789 (C -> T) to create a premature stop codon, and resulting in a truncated SPIA-1 protein of 26 aa (Fig 1C). Results obtained with *spia-1(syb7920)* phenocopied those obtained with *spia-1(fr179)* (Figs 1B and S1B). We further confirmed that the *spia-1*(*fr179)* mutation abrogates the PIA phenotype produced by RNA inactivation of any of the six furrow collagen genes (Figs 1D and S1C) but does not suppress the associated short size (i.e., the dumpy phenotype; S1D Fig). Moreover, we confirmed that *spia-1* mutation in furrow-less mutants reduced the endogenous expression of several AMPs genes including *nlp-29* (S1E Fig). Interestingly, we did not observe reduced *gst-4* nor *gdph-1* expression in *spia-1*, this latter one was even ~5 times increased (S1E Fig); these genes are respectively representative of the detoxification and osmotic stress responses kept in check by furrow collagens [12]. These data indicate that SPIA-1 is specifically required in the activation of the immune response upon furrow collagen loss.

In wild-type worms, *nlp-29* is expressed cyclically throughout development, possibly as a prophylactic protective mechanism following moulting [1,6,10]. We conducted a precise temporal analysis from the start of the L4 to the adult stage, using vulval shape as a proxy for developmental timing [23], as previously described [10,24]. In the *nlp-29*p::GFP reporter strain, we observed a peak of GFP production at the L4.2-L4.3 and young adult stages (Fig 1E and 1F). As observed before with this reporter upon fungal infection or wounding, we detect the GFP signal a few hours after the endogenous transcription [17]. This suggests a peak of *nlp-29* transcription a few hours before, which matches L3 & L4 moulting events respectively. A mutation in the transcription factor *sta-2* completely suppressed *nlp-29* induction, confirming that *sta-2* is required for the moulting-induced immune response (Fig 1E). In contrast, *spia-1(syb7920)* worms still presented both peaks and did not show any decrease in GFP production compared to wild-type worms (Fig 1E). In *dpy-7;spia-1(syb7920)*

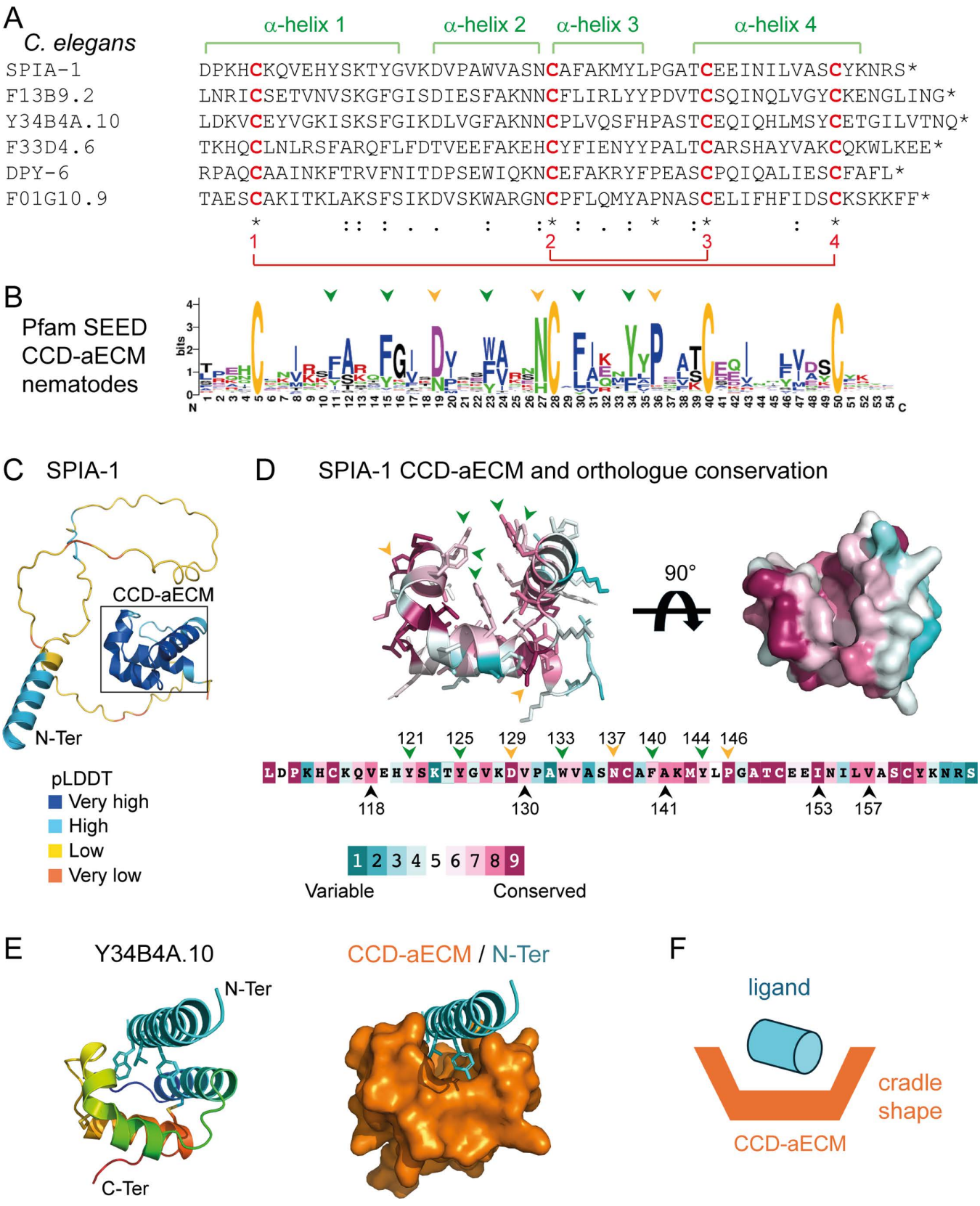

Fig 2. SPIA-1 is a secreted protein containing a novel cysteine-cradle domain. (A) In *C. elegans*, 6 proteins share a common and previously uncharacterised domain in their C-terminal region, of which the amino acid sequences are depicted. This domain contains 4 invariant cysteine residues predicted to

form two disulfide bridges (red) connecting 4 α-helices (green) and was named the cysteine cradle domain (CCD-aECM). (B) The sequence logo derived from the Pfam (PF23626) SEED alignment shows residues of the domain conserved across nematode homologues. The relative size of the residue letters indicates their frequency in the aligned sequences of the Pfam SEED. Arrows point to the aromatic residues lining the groove (green) and other highly conserved amino acids (yellow). (C) SPIA-1 structural model predicted with AlphaFold2 [27,65], rendered in cartoon and coloured according to the Predicted Local Distance Difference Test score (pLDDT), which indicates how well a predicted protein structure matches protein data bank structure information and multiple sequence alignment data: dark blue >90, light blue <90 & >70, yellow <70 & >50, orange <50. The CCD-aECM domain is framed in black. (D) Amino acid sequence (bottom) and AlphaFold prediction of the CCD-aECM rendered in a cartoon, with the side-chains shown as sticks (top left) or in surface with a 90° rotation (top right), and coloured according to the Consurf conservation scores [67] based on SPIA-1 orthologs alignment. Arrows point to the aromatic residues lining the groove (green), aliphatic residues that are in contact (black), and other highly conserved amino acids (yellow). Numbers indicate the position of the amino acid in the full-length SPIA-1. The predicted structural model of SPIA-1 CCD-aECM is also shown on S1 Movie. (E) The AlphaFold prediction model of Y34B4A.10 (left) is rendered in cartoon and coloured in rainbow (blue to red indicating the path of the polypeptide chain from N- to C-terminal end). Residues from the α-helix that are predicted to engage in hydrophobic interactions are shown as sticks. The same model rendered in surface (right) demonstrates how the N-terminal α-helix of Y34B4A.10 (cyan) is predicted to bind to the CCD-aECM groove of this protein (orange). (F) Simplified illustration of the proposed model for the interaction of the CCD-aECM with a ligand.

https://doi.org/10.1371/journal.pgen.1011593.g002

double mutants, although the PIA was reduced to levels qualitatively comparable to those in wild-type, as shown above, the moulting-induced peaks remained unaffected. Together, these results show that SPIA-1 is required in the furrow-less but not the moulting-induced immune responses.

spia-1 encodes a secreted protein with a novel cysteine-cradle domain

spia-1 is predicted to encode a secreted nematode-specific protein of 165 aa with no previously known function [25]. Its C-terminal region is annotated in the Panther database with a signature PTHR37435 that has no associated function [25,26]. This Panther family includes 5 other secreted *C. elegans* proteins: DPY-6, a mucin-like protein with a conserved role in cuticle formation [15], and 4 other uncharacterised nematode-specific proteins: F01G10.9, F13B9.2, Y34B4A.10 and F33D4.6 (Fig 2A). Orthologues of all 6 proteins are only present in nematodes, in free-living or in parasitic forms, and found in different clades, like *Rhabditina*, *Tylenchina* and *Spirurina*. These proteins have different lengths and contain regions with a compositional bias suggesting they may be largely intrinsically disordered, their common and most conserved part being located toward the C-terminus (Figs 2A and S2A). This common C-terminal region is predicted by AlphaFold2 [27] to adopt a globular structure composed of four α-helices. These α-helices are predicted to be arranged in two nearly orthogonal pairs, with two helices of one pair packed at both edges of the other and thus creating a cradle-shaped domain. This globular domain contains 4 invariant cysteines that define a sequence motif C_1-$(X)^{22}$-C_2-$(X)^7$-P-$(X)^3$-C_3-$(X)^9$-C_4. The cysteine residues are predicted to form two disulfide bonds connecting the α-helices, with C_1 bonding C_4 and C_2 bonding C_3 (Fig 2A and S1 Movie). These disulfide bonds are likely to play a structural role and be essential for the maintenance of the cradle-like shape of the domain (Fig 2C and 2D). Owing to its features, this domain was named 'aECM cysteine-cradle domain' (CCD-aECM or cysteine cradle domain) and its sequence diversity was added to the Pfam database [28] as a new entry PF23626.

The AlphaFold prediction of the cysteine cradle domain is in good agreement with predictions obtained using secondary structure and disulfide bond prediction programs which are based on different approaches [29–31]. The multiple sequence alignment of the cysteine cradle domain family (Fig 2D) or of the SPIA-1 orthologues in nematodes (Fig 2D) showed conserved features that strongly support the predicted structural model. In addition to the 4 invariant cysteine residues, these include: a highly conserved proline (Pro146 in SPIA-1) preceding and predicted to orient the α-helix 4, thus facilitating disulfide bond formation; two highly conserved aspartate/asparagine (Asp129 & Asn137 in SPIA-1) at both caps of α-helix

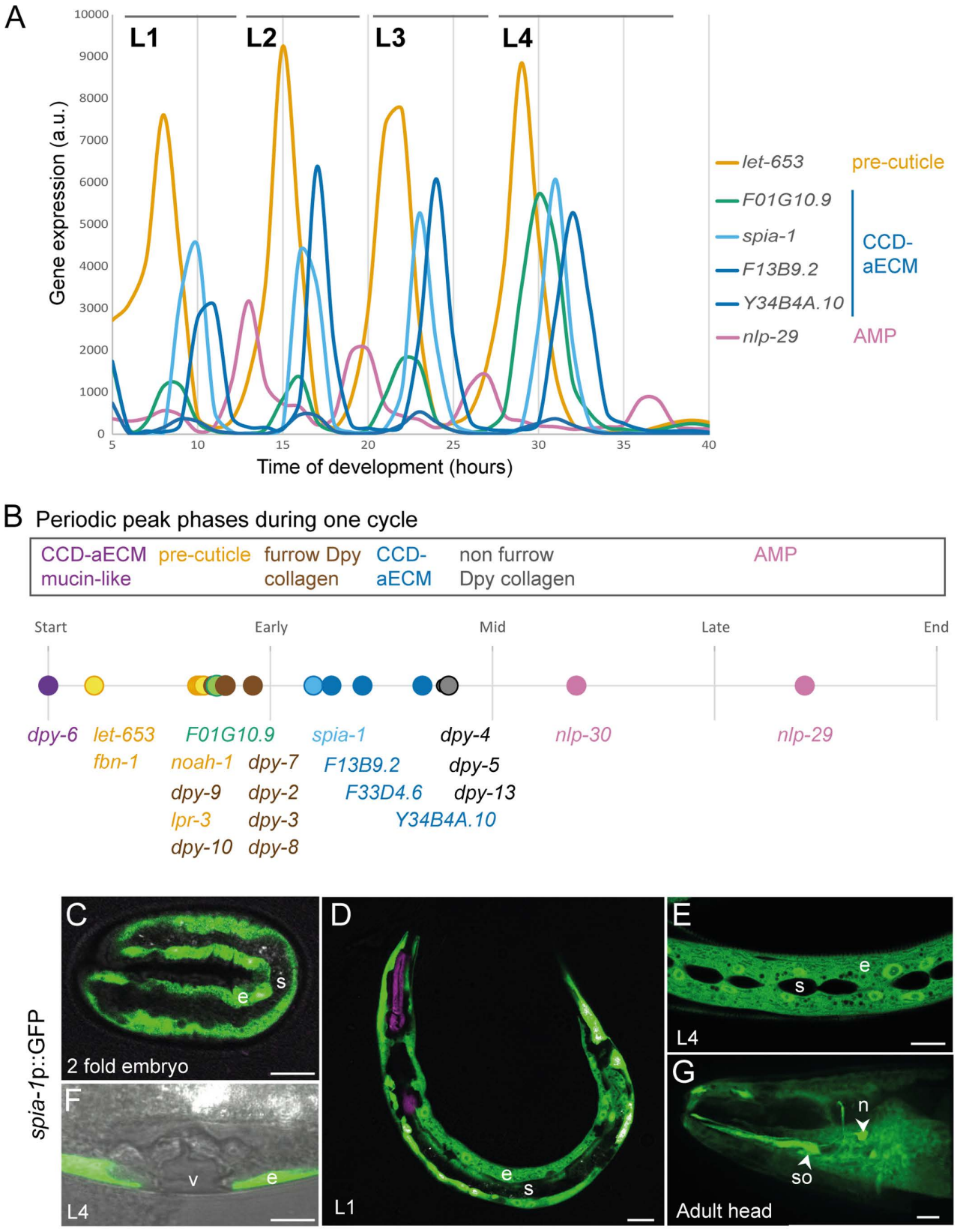

Fig 3. spia-1 is expressed in the epidermis and oscillatory between each moult. (A) AMP and aECM gene expression oscillates between each moult, with expression levels from an RNA-seq time course with 1-hour intervals between 5 and 40 hours after hatching, reanalysed from (Meeuse

et al. 2020) [37]. (B) Between each moult, a timeline of gene expression is represented, with *dpy-6* starting each cycle. Peak phase data reanalysed from (Meeuse *et al.* 2020). (C-G) Expression pattern of *spia-1* transcript in worms carrying the *frEx631[pSO22(spia-1*p::GFP*), myo-2*p::mCherry*]* transgene. Representative confocal images, n>5, of (C) 2-fold embryo, (D) L1 larva, (E, F) L4 larva, and (G) adult head. The signal is visible in the epidermis (e) at all stages, and also in head socket cell (so) and a neuron (n), but not in the seam cell (s), nor the vulva (v). Grey colour in (F) was acquired with a transmitted detection module; scale bar, 10 μm.

https://doi.org/10.1371/journal.pgen.1011593.g003

2 predicted to impose sharp turns of the polypeptide chain. In addition, hydrophobic interior interactions between conserved aliphatic residues, as well as hydrogen bonds (e.g., between Asn137 and the main-chain N-atom of Trp133 in SPIA-1), are predicted to stabilise the cysteine cradle domain. The residues constituting the groove are also semi-conserved suggesting they may be important for function (Fig 2B and 2D and S1 Movie). Moreover, aromatic residues line the groove: a prominent tryptophan located on α-helix 2 (Trp133 in SPIA-1), a phenylalanine (Phe140 in SPIA-1) and 3 tyrosines (Tyr121, Tyr125, Tyr144 in SPIA-1); they define a highly hydrophobic interface that could be involved in binding of unknown interaction partner(s). Interestingly, in the AlphaFold2 model of Y34B4A.10 (uniprot ID:Q8WSP0), an N-terminal α-helix of the protein itself docks into this groove (Fig 2E). A similar mode of interaction involving an α-helix docked into a hydrophobic groove has been previously observed; for example, between the p53 transactivation domain α-helix and the MDM2 cleft [32]. Alternatively, aromatic hydrophobic residues are also known to engage in binding of proline-rich peptides [33,34] suggesting another potential functional interaction in which the cysteine cradle domain might be involved (Fig 2F).

spia-1 is expressed in the epidermis and its expression oscillates during larval stages

During larval development, there are 4 moults spaced by ~7-8 hours during growth at 25°C. Genome-wide transcriptomic studies have revealed the rhythmic activity of thousands of genes that align with the moulting cycle. They follow a repeated pattern of oscillations in each cycle, peaking at a distinct point in each larval stage. A large proportion of the cycling genes are expressed in the epidermis and are suggested to be required for the formation of the new cuticle [35–39]. These oscillating transcripts include precuticle components that are only transiently present when the new cuticle is synthesised at intermolt and are endocytosed and degraded before each moult [1]. Analysing the data from [37,38], we observed that the transcripts for SPIA-1 and related proteins are part of these rhythmic oscillations (Fig 3A). We define that each cycle ended by the expression of AMPs, including *nlp-29*, which have been proposed to be induced to protect the epidermis while the old cuticle is shed [6], and that one of the first genes to start to oscillate in the early L1 is *dpy-6*. It encodes a protein that, in addition to its CCD-aECM, is enriched with tandem repeats of serine and threonine residues similar to those found in highly glycosylated mucins [15]. We then reanalysed the peak phase of genes that are known to be important for cuticle morphogenesis relative to *dpy-6*. All 5 genes encoding a CCD-aECM peak just after the pre-cuticle genes (orange) *let-653* and *fbn-1,* with *F01G10.9* (green) peaking together with the pre-cuticle genes *noah-1/2* & *lpr-3* and the 6 furrow Dpy collagens *dpy-2, dpy-3, dpy-7, dpy-8, dpy-9, dpy-10* (brown), followed by *spia-1, F13B9.2*, *F33D4.6* and *Y34B4A.10* (blue). These are then followed by the non-furrow collagens like *dpy-4, -5, -13* (black), and then the AMPs (pink) at the very end of each cycle (Fig 3B). The observation that CCD-aECM encoding genes cycle at the beginning of the new cuticle synthesis, together with precuticle and furrow collagen genes suggest a role in the formation of the new cuticle, including a very early role for *dpy-6*.

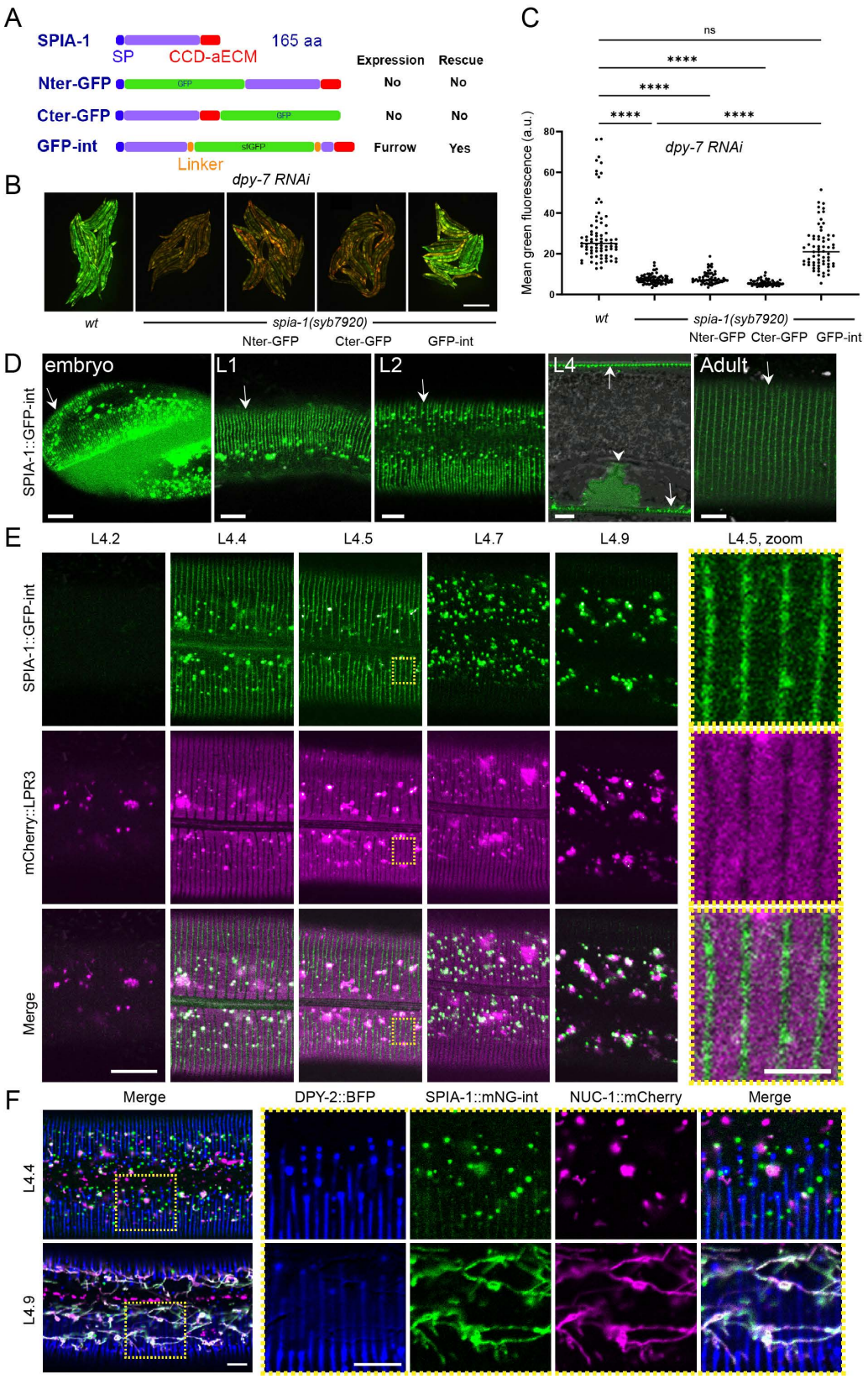

Fig 4. SPIA-1 localises to furrows. (A) Position of the insertion of GFP in each translational reporter with their expression pattern and rescue activities. For the KI strain, mNG is inserted at the same place as in GFP-int. (B-C) *spia-1*

mutation suppresses *nlp-29*p::GFP overexpression in *dpy-7* worms. The rescue of this suppression has been tested in *spia-1(syb7920)* young adults with the extra-chromosomal gene producing SPIA-1 tagged with GFP in Nter, Cter or internal position, in three independent experiments. (B) Representative images of one experiment; scale bar, 500 μm. (C) Relative green fluorescence is quantified (n=58-79); ****$p < 0.0001$. (D) Representative confocal images of the SPIA-1::sfGFP reporter (GFP-int) in 3-fold embryo, L1, L2, L4 vulval lumen and adult. We used a laser power ~2 times higher in adults compared to other stages (see S3A Fig). White arrows and arrowhead indicate signal in furrows and in vulval lumen, respectively; n>5, scale bar, 5 μm. (E) The L4 stage is subdivided into sub-stages in relation to the shape of the vulva, as previously described [23]. SPIA-1::sfGFP and mCherry::LPR-3 are observed in parallel. ~7 times magnification of the areas contained in the dashed rectangles are provided on the far right; scale bar, 10 μm (left), 2 μm (magnified area). (F) Representative confocal images of L4.4 (top) and L4.9 (bottom) larvae expressing DPY-2::BFP, SPIA-1::mNG-int, and NUC-1::mCherry. ~2.5 times magnification of the areas contained in the dashed rectangles are provided on the far right. Both single channels and the merge are shown; n>5, scale bar, 5 μm.

https://doi.org/10.1371/journal.pgen.1011593.g004

Targeted DamID studies are consistent with SPIA-1 expression in the epidermis hyp7 in larval stages [40]. In adult-specific single cell RNAseq, *spia-1* is also found expressed in cephalic and inner labial socket and phasmid sheath cells [41]. A transcriptional reporter confirmed that *spia-1* is expressed in the main epidermal cell and socket cells but is not visible in other epithelial cells like the seam cells, nor in the vulval cells (Fig 3C-G). The expression starts in embryos at the 2-fold stage, which is the time when pre-cuticle components like LPR-3 start to mark the cuticle, but later than the earliest components of the pre-cuticle sheath like NOAH-1 and FBN-1 (Fig 3C) [42–45]. The transcriptional reporter might be missing some of the endogenous regulation, but it includes 1.2 kb of upstream genomic sequence that harbours several predicted binding motifs for transcription factors, including NHR-23 that is important for oscillatory gene expression in epithelial cells [25,46,47]. Taken together these observations suggest that *spia-1* is expressed in epidermal cells and oscillates with a peak phase that follows the six furrow collagens and precuticle components.

SPIA-1 is localised to aECM periodic furrows

We tagged the SPIA-1 protein by insertion of GFP in 3 different positions: at the N-terminus after the signal peptide, at the C-terminus before the stop codon, or internally before the CCD-aECM. We introduced extra-chromosomal transgenes expressing these GFP-tagged SPIA-1 under the control of its own promoter into the *spia-1(syb7920)* mutant. Upon RNAi inactivation of *dpy-7*, the *spia-1(syb7920)* mutation suppressed the PIA phenotype; among the three transgenes, only the one containing the internally tagged SPIA-1::sfGFP (hereafter SPIA-1::sfGFP-int) rescued the PIA phenotype (Fig 4B and 4C). This is consistent with the lack of observable GFP signal in either of the 2 other strains. In contrast, the functional protein SPIA-1::sfGFP-int was visible in association with cuticle furrows starting in late embryonic stages and continuing throughout all larval stages (Fig 4D). We further generated a knock-in strain, IG2212, with SPIA-1 tagged with mNeonGreen (mNG) at the same position as the internal sfGFP. We confirmed that SPIA-1::mNG was located at furrows as it colocalised with DPY-2::BFP (S3B Fig). In both strains, SPIA-1 was still present in the adult, but more faintly (Figs 4D and S3A). We could not detect it in the shed cuticle, but this could be due to its low signal. In addition, SPIA-1 accumulated in the vulva lumen during the mid-L4 stage (Fig 4D). In accordance with its cyclic expression, the fluorescence intensity of furrow-associated SPIA-1 also cycled, peaking in the middle of the L4 larval stage (Fig 4E). SPIA-1 strongly accumulated in vesicles preceding each moult, like precuticular components. During the L4 larval stage, the precuticular lipocalin LPR-3 was shown to be only transiently present, being secreted from the L4.3 stage onwards, and observed in an annular pattern between L4.4 to L4.7 [48,49]. Using vulval shape as a proxy for developmental timing, as described previously, we observed that in a double labelled mCherry::LPR-3, SPIA-1::sfGFP-int strain,

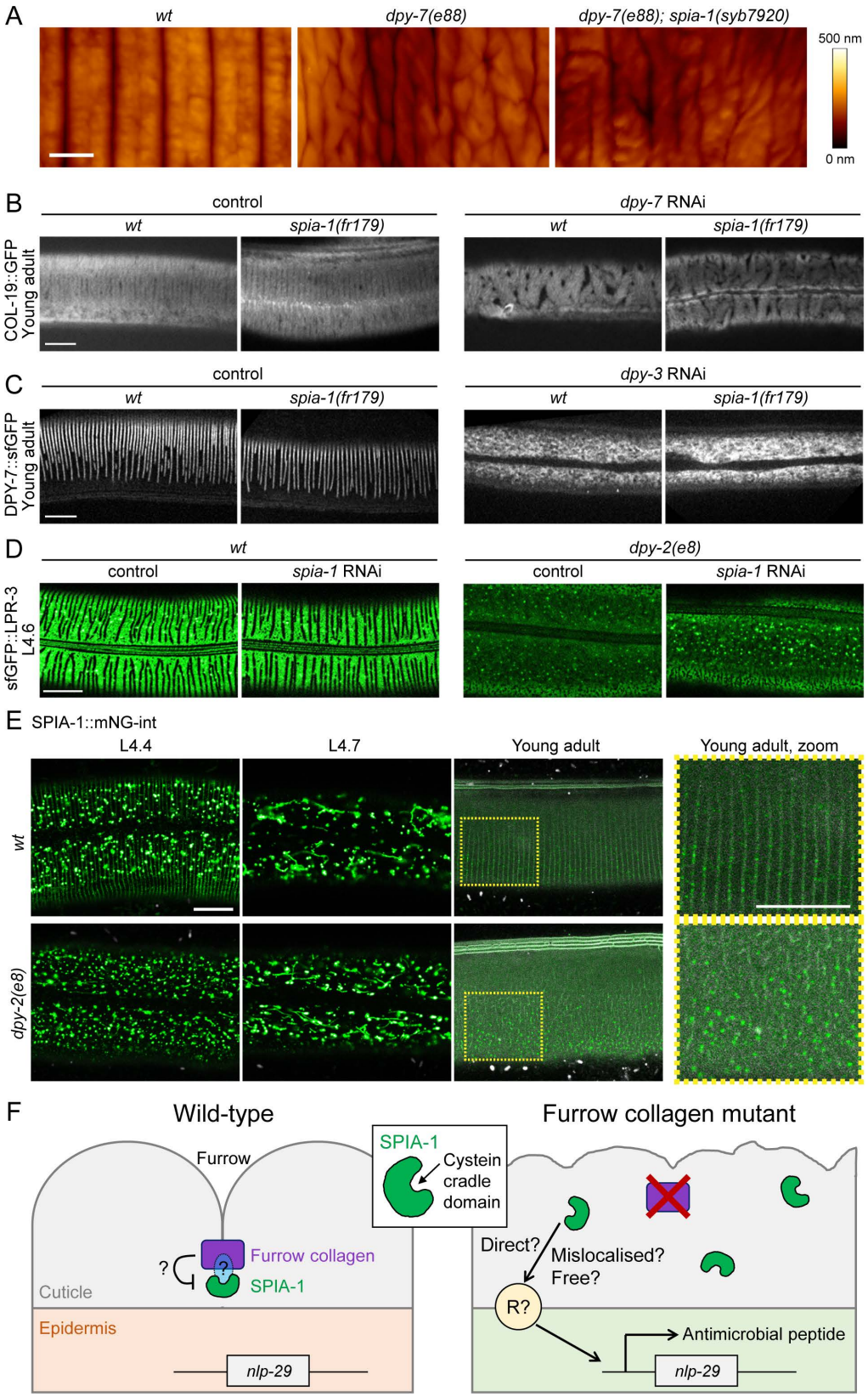

Fig 5. SPIA-1 acts downstream of furrow collagens. (A) AFM topography of the cuticle in wild-type, *dpy-7(e88)* and *dpy-7(e88); spia-1(syb7920)* young adult worms; n>3, scale bar, 1 μm. (B) *spia-1(fr179)* does not suppress

COL-19::GFP abnormal pattern following *dpy-7* RNAi. Representative images of *wt* or *spia-1(fr179)* young adults carrying COL-19::GFP treated with *sta-1* or *dpy-7* RNAi bacteria; n>5, scale bar, 10 μm. (C) *spia-1* does not suppress the absence of furrows following *dpy-3* RNAi; representative images of *wt* or *spia-1(fr179)* worms carrying DPY-7::sfGFP treated with *sta-1* or *dpy-3* RNAi bacteria; scale bar, 10 μm. (D) *spia-1* does not suppress the abnormal sfGFP::LPR-3 in *dpy-2(e8)*; representative images of *wt* or *dpy-2(e8)* L4.6 worms carrying sfGFP::LPR-3 treated with control (*sta-1)* or *spia-1* RNAi bacteria; scale bar, 10 μm. (E) SPIA-1::mNG-int is mislocalised in *dpy-2(e8)* mutants. Representative confocal images of the cuticle plane of *wt* or *dpy-2(e8)* L4.4, L4.7, or young adult worms carrying SPIA-1::mNG-int. We used a laser power ~2 times higher in adults compared to other stages, see S3A Fig. A ~2.5 times magnification of the areas contained in the dashed rectangles is provided on the far right; n>5, scale bar, 10 μm. (F) Cartoon presenting the proposed model for SPIA-1 activity in wild-type or furrow-less adults. Not to scale. SPIA-1 could bind directly or indirectly to furrow collagens. In the absence of furrow collagens, SPIA-1 may become unbound, allowing it to directly or indirectly activate signalling in the epidermis.

https://doi.org/10.1371/journal.pgen.1011593.g005

SPIA-1 started to be visible at the L4.4 stage, at furrows in a pattern complementary to LPR-3, and in fluorescent vesicles (Fig 4E). Its level at the furrows then decreased, while it remained in vesicles throughout the end of the L4 stage.

The intermolt peak and strong accumulation of SPIA-1 in vesicles before moulting resembled that of precuticular components like LPR-3 [43,48]. Furthermore, we saw that SPIA-1::sfGFP-int and mCherry::LPR-3 vesicles partly overlapped (Fig 4E). To study further the nature of the SPIA-1 transient fluorescent vesicles, we combined SPIA-1::mNG with the lysosomal hydrolase NUC-1::mCherry that served as an endosomal and a lysosomal reporter, as previously described [50] and the DPY-2::BFP reporter to mark the furrows. Interestingly, in early L4, while NUC-1, SPIA-1 and DPY-2 are each visible in fluorescent vesicles, most of these were independent (Fig 4F). This suggests that SPIA-1 and DPY-2 are initially not associated with the same trafficking compartments, even though they colocalise at furrows once secreted in the matrix, and might be secreted in different ways. Remarkably, in late L4, most SPIA-1::mNG and NUC-1 fluorescent vesicles adopted a tubular structure, characteristic of lysosomal compartments, and appeared mostly colocalised (Fig 4F). It is interesting to note that these lysosomal tubular structures are visible with the mNG but not sfGFP tagged SPIA-1 strain, which presumably reflect the quenching of the latter's fluorescence in acidic compartments. Overall, these data suggest that, in late L4, SPIA-1 is directed to lysosomes for degradation, a mark of precuticular components. This is also consistent with its reduced presence at furrows at the adult stage.

Altogether, these data suggest that SPIA-1 is an atypical cuticle component that shares some temporal and trafficking features of pre-cuticle, where its matrix signal peaks in the intermolt period of cuticle synthesis, after which most of it is cleared by endocytosis. Interestingly, the secreted hedgehog-related protein GRL-7, one of the few known components to be specifically positioned at the furrows in the pre-cuticle, contains a ground-like nematode-specific domain, which is another type of cysteine domain. It has been suggested to have a signalling role related to matrix association [1,51,52].

SPIA-1 acts downstream of furrow collagens

spia-1 was identified as a suppressor of the persistent immune activation provoked by the absence of furrows. Although *spia-1* did not reverse the Dpy phenotype of furrow-less mutants, it conceivably exerted its suppressive function by restoring normal furrow morphology. We examined the cuticle of worms deficient for different furrow collagens in the *spia-1* background with atomic force microscopy (AFM). As previously described [10], the AFM imaging mode can reveal periodic and regular furrows in wild-type young adult worms and a highly irregular, wrinkled appearance with variable depth in furrow-less mutants (Fig 5A). The topography of the *spia-1 dpy-7* double mutants was not restored to wild type (Fig 5A). We

further confirmed this phenotype with a COL-19::GFP marker and a DPY-7::sfGFP marker. In no case did the *spia-1* mutation restore furrows (Fig 5B and 5C). We noticed that when furrows are absent in a *dpy-2* mutant, the precuticle component LPR-3 cannot assemble anymore in its specific anti-furrow pattern during the mid L4, as visualised with sfGFP::LPR-3. The absence of *spia-1* could not restore the correct LPR-3 localisation in furrow-less mutants (Fig 5D). The absence of *spia-1* did not affect cuticle collagen DPY-7 or COL-19 nor precuticle LPR-3 localisation in an otherwise wild-type background (Fig 5B-D). Together, these observations indicate that *spia-1* acts downstream of the patterning and signalling roles of the furrow collagens.

We then investigated SPIA-1 localisation in a furrow-less context, either in a *dpy-2* mutant or by RNAi inactivation of *dpy-7* (Figs 5E and S4). Furrow-less mutant conserved the vesicular and tubular pattern of SPIA-1 in L4 in the epidermis, and SPIA-1 was still present in the cuticle, suggesting that SPIA-1 was correctly produced, transported and degraded. However, in both L4 and adult, the furrowed pattern of SPIA-1 was lost and replaced by a signal randomly distributed in the cuticle (Fig 5E). We confirmed that the inactivation of any of the 6 furrow collagens, here *dpy-3*, impacts the localisation of other furrow collagens in the cuticle (Fig 5C) [4]. Thus, SPIA-1, like LPR-3, requires the presence of furrow collagens in the cuticle for its proper matrix localisation.

A model for the role of SPIA-1 and its novel CCD-aECM domain

We propose a dual role of SPIA-1 as an atypical precuticular component of the furrow, as well as a cuticular mediator of cuticle damage. SPIA-1 shares characteristics of precuticular components as it is present at intermolt and highly endocytosed and degraded in lysosome before moulting. But unlike other characterised precuticular components, SPIA-1 is still present in the adult cuticle. Precuticular and some cyclic cuticular components like furrow collagens, are suggested to have a role in patterning the new cuticle ([1,10,48], Fig 5B-D). In the absence of SPIA-1, we observed no obvious phenotype associated with cuticle morphogenesis, nor in patterning the precuticle LPR-3 or furrow collagens. Although this could mean that it has no role in cuticle morphogenesis, SPIA-1 could act redundantly, potentially with other cysteine cradle domain proteins. All the cysteine cradle domain proteins including SPIA-1 are only found in nematodes and predicted to be secreted. They are encoded by genes that have a cyclic expression and are predicted or already demonstrated to be expressed in the epidermis [25,38,40,41]. Altogether, these strongly suggest that all 6 cysteine cradle domain proteins are matrix proteins of the specialised nematode cuticle, hence the name of CCD-aECM for this novel Pfam domain.

SPIA-1 is required for the immune response provoked by the loss of furrows. In furrow-less mutants, we showed that SPIA-1 is aberrantly localised in the cuticle. The mislocalisation of SPIA-1 could trigger the persistent immune response in the epidermis. In normal circumstances, SPIA-1 could be muted by being directly or indirectly bound to collagen, thereby preventing it from signalling damage. In the absence of furrow collagen, it would be free to interact with unknown components, in parallel to the DCAR-1/GPA-12 pathway, to activate an immune response (Fig 5F). One hypothesis is that SPIA-1 could be directly linked to furrow collagens via its CCD-aECM. SPIA-1 activation of the immune response could also be indirect, e.g., if SPIA-1 was required for the presence or sensor activity of another molecule. While 4 of the CCD-aECM proteins have not been studied yet, it is interesting to report that when endogenously tagged with mNG, DPY-6 is observed at furrows in the cuticle (S5 Fig). Further investigations would be required to understand the potential role for CCD-aECM proteins in building a functional aECM and monitoring cuticle integrity.

Materials and methods

EMS suppressor screen and mutation identification

P0 from the strain IG1389 *frIs7[nlp-29*p::GFP, *col-12*p::DsRed*] IV; frIs30[(col-19p::GPA-12gf), pNP21(pBunc-53::GFP)]* were mutagenised with EMS as previously described [7,22]. Individual synchronised F2 L1 worms were plated on *dpy-7* RNAi plates. Late larval F2 that showed a low expression of *nlp-29*p::GFP were cloned. The ones that then showed a higher GFP expression at adult stage were further analysed. As a positive control for the mutagenesis, several candidates that still abrogate the GFP signal at the adult stage were also cloned, and led to the isolation of several new Nipi alleles including *snf-12(fr189)*. *spia-1* was further back-crossed with IG274 *frIs7* and a dozen of F2 without the GPA-12gf were isolated, then pooled and send for whole-genome sequencing (BGI). Sequences were analysed with MiModD v0.1.9, https://mimodd.readthedocs.io/en/latest, based on CloudMap [53], using the sub-commands *varcall*, then *varextract* and finally *annotate*. This later step required SnpEff v5 and the SnpEff database *WBcel235.86*. The VCF file produced was re-formatted using a Python script to allow the curation of all putative mutations with user-defined thresholds.

Nematode strains

All *C. elegans* strains were maintained on nematode growth medium (NGM) and fed with *E. coli* OP50, as described [54]. Tab A in S1 Table shows a list of the strains used in this study, including those previously published: BE93 *dpy-2(e8) II* [8], IG1060 *sta-2(ok1860) V; frIs7[nlp-29p::GFP, col-12p::DsRed] IV* [11], IG1689 *dpy-7(e88) X; frIs7[nlp-29p::GFP, col-12p::DsRed] IV*[12], UP3666 *lpr-3(cs250[ssSfGFP::LPR-3]) X* & UP3808 *lpr-3(cs266[mCherry::LPR-3]) X* [48], IG1389 *frIs7[nlp-29p::GFP, col-12p::DsRed] IV; frIs30[(col-19p::GPA-12gf), pNP21(pBunc-53::GFP)] I* & IG1392 *sta-2(ok1860) V; frIs7[nlp-29p::GFP, col-12p::DsRed] IV; frIs30[(col-19p::GPA-12gf), pNP21(pBunc-53::GFP)] I*(19), XW18042 *qxSi722[dpy-7p::DPY-7::sfGFP] II* & XW5399 *qxIs257[ced-1p::NUC-1::mCherry, unc-76(+)] V* [50], IG274 *frIs7[col-12p::DsRed, nlp-29p::GFP] IV; fln-2(ot611) X* [7], TP12 *kaIs12[COL-19::GFP]* [9], IG1426 *dcar-1(tm2484) V; frIs7[nlp-29p::GFP, col-12p::DsRed] IV; frIs30[(col-19p::GPA-12gf), pNP21(pBunc-53::GFP)] I* [14] and HW1371 *xeSi137[F33D4.6p:: gfp::h2b::pest::unc-54 3'UTR; unc-119 +] I* [38]. Strains with extrachromosomal hygromycin resistance genes were selected on NGM plates supplemented with 0.3 mg/ml hygromycin B (Sigma-Aldrich).

Constructs and transgenic lines

All following constructs were made using SLiCE [55] and the plasmid editor Ape [56] and all primer sequences used to generate specific PCR amplicons are in Tab B in S1 Table. A transcriptional construct (pSO22), was generated by cloning a PCR amplicon (3321-3322) containing 1.23 kb upstream of the *spia-1* start codon into pPD95.75 [57]. To create translational constructs, GFP was inserted in *spia-1* either at the C-terminal end (pSO24: 3326-3327) or after the N-terminal signal peptide (pSO25: 3366-3367, 2093-3365). Internal tag translational construct (pSO26) was generated by inserting the sfGFP (kindly provided by A. Golden and H. Smith) in SPIA-1 at position 92 flanked with N-tag and C-tag linker used in pMLS288 and pMLS287 respectively [58] (3392-3393, 3394-3395).

pSO22 was injected at the concentration of 50 ng/µl with the co-injection marker *ttx-3*p::RFP at 50 ng/µl into N2 to get IG1986 and the co-injection marker *myo-2*p::mCherry at 2 ng/µl into N2 to get IG1988. Translational constructs (pSO24, pSO25, or pSO26) were injected at the concentration of 2 ng/µl, with the co-injection marker *myo-2*p::mCherry at 2 ng/µl and the HygR selection plasmid pZX13 at 50 ng/µl with pKS at 50 ng/µl into N2 (pSO24 and pSO25), or IG2093 *spia-1(fr179)* (pSO26) to get IG1999, IG2062, IG2108 respectively.

The strain PHX7920 *spia-1(syb7920)* generated by CRISPR editing (SunyBiotech), has a deletion of 710 bp (bp 79-788) in *spia-1* and a modification of bp 78 (C -> **T**) to create a premature stop codon. The sequence from the **ATG** to the original **stop** codon is ATGAAGCTAGTTGTTGTTTTGGCTTGTCTTGTTGTAGTAGCTGAGGCTTAT-TCAAAATCTGGAAATCCATACAAGACT**T**AACTTGTGAGGAGATTAACATTTTGGT-GGCCTCTTGCTACAAGAACAGAAGC**TAA**, resulting in a truncated SPIA-1 protein of 26 aa. All the transgenic strains carrying *spia-1(fr179)* or *spia-1(syb7920)* were obtained by conventional crosses and genotypes were confirmed by sequencing (see Tab A in S1 Table for a list of all strains).

The strain IG2212 *spia-1(fr201(SPIA-1internal mNG^SEC^::3xFLAG))* was generated by CRISPR editing using a self-excising cassette as previously described [59]; *mNG^SEC^::3x-FLAG* was inserted at the same position than the GFP in pSO26. A repair template was constructed using Gibson cloning to insert a 622 bp 5' homology arm and a 575 bp 3' homology arm into an *Avr*II+*Spe*I digested pDD268 backbone [59] to make pJW2521. A sgRNA vector (pJW2568) targeting the ATCGGAAACAGTTGGTGGAG TGG sequence (PAM underlined, not included in vector) was made through SapTrap [58], by cloning of an annealed oligo pair into pJW1839. Wild-type N2 animals were injected with pJW2568, pJW2521, a pCFJ2474 Cas9 plasmid, a *mlc-1*p::mNG co-injection marker (pSEM229), and a *snt-1*p::HisCl (pSEM238) counter selection marker [60–62]. Plates were flooded with hygromycin and histamine as previously described [59]. A hygromycin-resistant, rolling strain [JDW774 *spia-1 ((spia-1(spia-1 internal mNG^SEC^::3xFLAG)) X*] was recovered and then the self-excising cassette was removed through heat-shock as described in [59] to create IG2212. The strain MCP597 *dpy-2(bab597[DPY-2::mTaqBFP2]) II* was obtained by Segicel, by adding BFP at the C-terminus of DPY-2. Note that in the 3'utr, 2 bases have been deleted in this allele and the sequence after the stop codon is TAGttgattctctctgatccttttg instead of TAGttgattctctctg-**c**atcc**t**tttttg. The strain PHX3742 *dpy-6(syb3742(DPY-6::mNG))* was obtained by SunyBiotech, by adding mNG at the C-terminus of DPY-6. All knock-in strains were confirmed by PCR genotyping using primers outside the homology arms and Sanger sequencing.

Sequence analyses

The following *C. elegans* CCD-aECM proteins (WormBase geneID/UniProt ID) SPIA-1/Q19281, Y34B4A.10/Q8WSP0, F33D4.6/O44189 (long isoform with the CCD-aECM), DPY-6/Q94185, F01G10.9/O17767 and F13B9.2/Q19385, were analysed with BlastP [63], WormBase [25], Panther [26], Pfam [28], Interpro [64] and AlphaFold2 & 3 [27,65]. We built the Pfam family PF23626 (named 'aECM cysteine-cradle domain') using sequences of CCD-aECM paralogues with domain boundaries defined based on the AlphaFold2 prediction models; Pfam PF23626 is available since the Pfam release 37.1. We iteratively searched for homologues using the HMMER package [66] and used an inclusion threshold of 27 bits. SPIA-1 orthologues including PIC17963.1 [*Caenorhabditis nigoni*], CAI5454296.1 [*Caenorhabditis angaria*], WKY17175.1 [*Nippostrongylus brasiliensis*], VDO70284.1 [*Heligmosomoides polygyrus*], EPB77628.1 [*Ancylostoma ceylanicum*], CDJ96309.1 [*Haemonchus contortus*], XP_013305412.2 [*Necator americanus*], KAF8381298.1 [*Pristionchus pacificus*], KAK5976273.1 [*Trichostrongylus colubriformis*], KAI6173309.1 [*Aphelenchoides besseyi*] were used for alignment and Consurf conservation scores [67].

RNA interference

RNAi bacterial clones were obtained from the Ahringer library [68] and verified by sequencing (see Tab C in S1 Table). RNAi bacteria were seeded on NGM plates supplemented with

100 g/ml ampicillin and 1 mM Isopropyl-β-D-thiogalactopyranoside (IPTG). Worms were transferred onto RNAi plates as L1 larvae and cultured at 25 °C until L4 or young adult stage. In all our experiments, we use *sta-1* as a control, as we have shown over the last decade that it does not affect the development nor any stress or innate response in the epidermis [11,14,17,19,69].

*nlp-29*p::GFP fluorescent reporter analyses

Representative fluorescent images including both green (*nlp-29*p::GFP) and red (*col-12*p::DsRed) fluorescence were taken of *frIs7* transgenic worms mounted on a 2% agarose pad on a glass slide, anaesthetised with 1 mM levamisole in 50 mM NaCl, using the Zeiss AxioCam HR digital colour camera and AxioVision Rel. 4.6 software (Carl Zeiss AG). For quantification, the same worms were manually isolated and imaged again. Each worm was computationally contoured on ImageJ, by successively applying the RenyiEntropy threshold method provided by the plugin CLIJ2 [70] to the red image, converting the grayscale image to binary, suppressing noise (binary open), filling holes, and creating masks (analyze particles). Masks were applied to the original images, systematically controlled by eye, and corrected if needed. Mean green fluorescence signal was further measured for each contoured worm.

In S1C and S1D Fig, *nlp-29*p::GFP expression was quantified with the COPAS Biosort (Union Biometrica; Holliston, MA) as described in [22]. In each case, the results are representative of at least three independent experiments with more than 70 worms analysed. The ratio between GFP intensity and size (time of flight) is represented in arbitrary units.

Atomic force microscopy

As previously described [10], the worms were paralysed in 15 mg/mL 2,3-butanedione monoxime (BDM, Sigma) for 10-30 min. They were then aligned on a ~2-mm-thick 4% freshly prepared agarose pad in a Petri dish (30 mm diameter). For full immobilisation, the worms were fixed (head and tail) with 2% low-melting agarose (GibcoBRL) instead of glue, as we found that the latter altered the cleanliness of the topographic image. After the agarose dried, we immersed again the worms in the BDM solution. AFM data were obtained using a NanoWizard4 (Bruker-JPK) during up to one hour following mounting. 10×10 μm areas on top of the worms were scanned using PFQNM-LC-cal cantilevers (Bruker) in quantitative imaging mode. The inverse of the optical lever sensitivity (invOLS) was calibrated from the thermal spectra in liquid, using the pre-calibrated spring constant of the cantilevers and the correction factors described in [71]. The force setpoint was set at 0.5 nN, speed at 50 μm/s and the range at 100 nm in Z. All topographical images (256×256 px) are flattened using the plane fitting and line levelling options of the JPK software to correct for sample tilt.

Confocal microscopy

Worms were mounted on a 2% agarose pad, in a drop of 1 mM levamisole in 50 mM NaCl. Images were acquired during the following 60 min, using Zeiss confocal laser scanning microscopes (LSM780, 880 or 980) and the acquisition software Zen with a Plan-Apochromat Oil DIC M27 40×/1.4 or 63×/1.40 objective. Pinhole size was set to 1 AU. Samples were illuminated with 405 nm (BFP), 488 nm (GFP, mNG) and 561 nm (mCherry) with varied laser power based on protein abundance and tissue imaged, with 4 lines accumulation and 750 gain settings. Spectral imaging combined with linear unmixing was used to separate the autofluorescence of the cuticle. In all images, only one confocal plane is presented.

Quantitative PCR

Total RNA samples were obtained by Trizol (Invitrogen)/chloroform extraction. One mg of total RNA was then used for reverse transcription (Applied Biosystems). Quantitative real-time PCR was performed using 1 µl of cDNA in 10 µl of SYBR Green (Applied Biosystem) and 0.1 mM of primers on a 7500 Fast Real-Time PCR System using *act-1* as a reference gene. Primer sequences are provided in Tab B in S1 Table.

Statistical analysis

Data were analysed with the GraphPad Prism 10.3 software. Statistical differences between groups were determined by the Kruskal-Wallis' test followed by the Dunn's test. Data were considered significantly different when *p*-value was less than 0.05.

Supporting information

S1 Fig. Suppressor screen design and expected outcome and quantification of *spia-1* mutant phenotype in different conditions. (A) In the suppressor screen, we triggered a PIA in the strain IG1389 by inactivating *dpy-7* by RNAi (left). In this strain, the state of the immune response is monitored (*frIs7* construct; green fluorescence off=inactive, green fluorescence on=active) and GPA-12 is constitutively active in the adult (*frIs30*). Different scenarios are expected depending on the gene affected after EMS-induced mutagenesis (right). (B) Quantification of relative green fluorescence in worms carrying *frIs7* and *frIs30* constructs, but without *dpy-7* RNAi inactivation, in L4 and young adults (yAd); n>14. Only the inactivation of a gene acting downstream of GPA-12 (e.g., *sta-2*) leads to the suppression of the green fluorescence in adults. (C-D) Quantification with the Biosort of the ratio between *nlp-29*p::GFP intensity and size (C) and of the size of the worms (D) in *wt* or *spia-1(fr179)* adults following RNAi inactivation of the 4 furrow collagen genes and the *sta-1* control; n>70, one of 3 independent experiments. *spia-1(fr179)* does not suppress the short size induced via inactivation of the 4 furrow collagen genes. Statistical comparisons were made by comparing to the corresponding *sta-1* control. ***p* < 0.01; *****p* < 0.0001. (E) mRNA levels of *nlp-29*, *nlp-34*, *cnc-2*, *cnc-4*, *gst-4* and *gpdh-1* were quantified by qPCR in wild-type and *spia-1(fr179)* worms upon RNAi inactivation of *sta-1* or *dpy-7*, in three independent experiments. The mean fold-changes between the *dpy-7* and *sta-1* levels are represented. In *spia-1(fr179)*, the transcription of AMPs genes including *nlp-29, nlp-34* and *cnc-4* were reduced, contrary to the transcription of *gst-4* and *gpdh-1*, the latter being increased.
(TIF)

S2 Fig. Domain organisation as annotated in InterPro and structural models predicted with AlphaFold of the 6 CCD-aECM proteins in *C. elegans*. (A) Domain organisation of the 6 CCD-aECM proteins in *C. elegans*, as annotated in InterPro [28,64] and (B) structural models predicted with AlphaFold [27,65], rendered with the Predicted Local Distance Difference Test score (pLDDT), which indicates how well a predicted protein structure matches protein data bank structure information and multiple sequence alignment data.
(TIF)

S3 Fig. SPIA-1::sfGFP and SPIA-1::mNG in L4 and adult. (A) The confocal image of the SPIA-1::sfGFP reporter (GFP-int) in the adult shown in Fig 4D is presented aside from a representative adult wild-type imaged using same illumination conditions; n>5, scale bar, 5 µm. (B) Zoom on the furrows in the L4.4 shown in Fig 4F. Both single channels and the merge are shown, as depicted. NUC-1::mCherry is not shown for clarity; scale bar, 5 µm.
(TIF)

S4 Fig. SPIA-1::mNG-int young adults following *dpy-7* RNAi inactivation. Representative images of SPIA-1::mNG-int young adults following *dpy-7* RNAi inactivation. To compare with Fig 5E. A ~2.5 times magnification of the area contained in the dashed rectangle is provided on the far right; n>5, scale bar, 10 μm.
(TIF)

S5 Fig. Furrow localisation of DPY-6::mNG-int. Representative fluorescent images of the furrow localisation of DPY-6::mNG-int, in a L1 (top) or L2 larva (bottom); n>5, scale bar, 20 μm (top), 10 μm (bottom).
(TIF)

S1 Movie. AlphaFold2 prediction of the SPIA-1 conserved CCD-aECM rendered in surface and cartoon. The model is coloured according to Consurf conservation scores across SPIA-1 orthologues in nematodes. The movie features the invariant cysteine residues predicted to form disulfide bonds (Cys138 with Cys150, Cys115 with Cys160), residues involved in hydrogen bonds probably stabilising the CCD-aECM (Trp133 with Asn137, Asp129 with Ala132, Leu110 with Ser159), aromatic residues lining the groove and defining a highly hydrophobic interface (Tyr121, Tyr125, Trp133, Phe140, Tyr144), and other conserved residues with predicted structural and functional roles (Gly126, Asp129, Pro146). Numbers indicate the position of the amino acid in the *C. elegans* SPIA-1 protein sequence.
(MP4)

S1 Table. This table includes all the worm strains, the construct and primers and RNAi clones used in this study.
(XLSX)

S1 Data. This table contains the raw data presented in all the graphs in this study.
(XLSX)

Acknowledgments

We thank Damien Courtine for the installation and use of MiModD, Ebrima Bojang and Sarah Sharkaoui for participation in the genetic screen that identified *spia-1*, Matt Ragle, Emma Cadena, Jack Clancy for cloning and injections, Mathieu Fallet for help in image quantifications. We thank Andy Golden and Harold Smith for sending us the sfGFP plasmid, Margaux Gibert and SEGiCel (SFR Santé Lyon Est CNRS UAR 3453, Lyon, France) for the DPY-2::BFP strain. The Fire Lab *C. elegans* Vector Kit was a gift from Andrew Fire (Addgene kit # 1000000001). Worm sorting was performed by Jérôme Belougne using the facilities of the French National Functional Genomics platform, supported by the GIS IBiSA and Labex INFORM. Some *C. elegans* strains were provided by the CGC, funded by NIH Office of Research Infrastructure Programs (P40 OD010440). We thank Tim Schedl, Stavros Diamantakis and the staff at WormBase for amazing community work including the maintenance of a curated database, Meera Sundaram, Jonathan Ewbank, Michel Labouesse and Helge Großhans for discussions and comments on the manuscript. We acknowledge the PICSL imaging facility of the CIML (ImagImm), member of the national infrastructure France-BioImaging supported by the French National Research Agency ANR-24-INBS-0005 FBI (BIOGEN).

Author contributions

Conceptualization: Nathalie Pujol.

Formal analysis: Thomas Sonntag, Shizue Omi, Antonina Andreeva.

Funding acquisition: Nathalie Pujol.

Investigation: Thomas Sonntag, Shizue Omi, Antonina Andreeva, Claire Valotteau, Jeanne Eichelbrenner, Nathalie Pujol.

Methodology: Thomas Sonntag, Shizue Omi, Antonina Andreeva.

Resources: Andrew D Chisholm, Jordan D. Ward.

Writing – original draft: Nathalie Pujol.

Writing – review & editing: Thomas Sonntag.

References

1. Sundaram MV, Pujol N. The *Caenorhabditis elegans* cuticle and precuticle: a model for studying dynamic apical extracellular matrices in vivo. Genetics. 2024;227(4):iyae072. https://doi.org/10.1093/genetics/iyae072 PMID: 38995735
2. Adams J, Pooranachithra M, Jyo E, Zheng S, Goncharov A, Crew J. Nanoscale patterning of collagens in *C. elegans* apical extracellular matrix. Nature Communications. 2023;14(1):7506. PMID: 37980413
3. Cox GN, Kusch M, Edgar RS. Cuticle of *Caenorhabditis elegans*: its isolation and partial characterization. J Cell Biol. 1981;90(1):7–17. https://doi.org/10.1083/jcb.90.1.7 PMID: 7251677
4. McMahon L, Muriel JM, Roberts B, Quinn M, Johnstone IL. Two sets of interacting collagens form functionally distinct substructures within a *Caenorhabditis elegans* extracellular matrix. Mol Biol Cell. 2003;14(4):1366–78. https://doi.org/10.1091/mbc.e02-08-0479 PMID: 12686594
5. Lažetić V, Fay DS. Molting in *C. elegans*. Worm. 2017;6(1):e1330246. https://doi.org/10.1080/21624054.2017.1330246 PMID: 28702275
6. Martineau CN, Kirienko NV, Pujol N. Innate immunity in *C. elegans*. Curr Top Dev Biol. 2021;144:309–51. https://doi.org/10.1016/bs.ctdb.2020.12.007 PMID: 33992157
7. Pujol N, Cypowyj S, Ziegler K, Millet A, Astrain A, Goncharov A, et al. Distinct innate immune responses to infection and wounding in the *C. elegans* epidermis. Curr Biol. 2008;18(7):481–9. https://doi.org/10.1016/j.cub.2008.02.079 PMID: 18394898
8. Cox GN, Laufer JS, Kusch M, Edgar RS. Genetic and Phenotypic Characterization of Roller Mutants of *Caenorhabditis elegans*. Genetics. 1980;95(2):317–39. https://doi.org/10.1093/genetics/95.2.317 PMID: 17249038
9. Thein MC, McCormack G, Winter AD, Johnstone IL, Shoemaker CB, Page AP. *Caenorhabditis elegans* exoskeleton collagen COL-19: an adult-specific marker for collagen modification and assembly, and the analysis of organismal morphology. Dev Dyn. 2003;226(3):523–39. https://doi.org/10.1002/dvdy.10259 PMID: 12619137
10. Aggad D, Brouilly N, Omi S, Essmann C, Dehapiot B, Savage-Dunn C. Meisosomes, folded membrane microdomains between the apical extracellular matrix and epidermis. Elife. 2023;12:e75906. PMID: 36913486 https://doi.org/10.7554/eLife.75906
11. Dierking K, Polanowska J, Omi S, Engelmann I, Gut M, Lembo F, et al. Unusual regulation of a STAT protein by an SLC6 family transporter in *C. elegans* epidermal innate immunity. Cell Host Microbe. 2011;9(5):425–35. https://doi.org/10.1016/j.chom.2011.04.011 PMID: 21575913
12. Dodd W, Tang L, Lone J-C, Wimberly K, Wu C-W, Consalvo C, et al. A Damage Sensor Associated with the Cuticle Coordinates Three Core Environmental Stress Responses in *Caenorhabditis elegans*. Genetics. 2018;208(4):1467–82. https://doi.org/10.1534/genetics.118.300827 PMID: 29487136
13. Pujol N, Zugasti O, Wong D, Couillault C, Kurz CL, Schulenburg H, et al. Anti-fungal innate immunity in *C. elegans* is enhanced by evolutionary diversification of antimicrobial peptides. PLoS Pathog. 2008;4(7):e1000105. https://doi.org/10.1371/journal.ppat.1000105 PMID: 18636113
14. Zugasti O, Bose N, Squiban B, Belougne J, Kurz C, Schroeder F, et al. Activation of a G protein-coupled receptor by its endogenous ligand triggers the innate immune response of *C. elegans*. Nature Immunology. 2014;15(9):833–8. PMID: 25086774
15. Sun S, Theska T, Witte H, Ragsdale EJ, Sommer RJ. The oscillating Mucin-type protein DPY-6 has a conserved role in nematode mouth and cuticle formation. Genetics. 2022;220(3):iyab233. https://doi.org/10.1093/genetics/iyab233 PMID: 35088845
16. Couillault C, Pujol N, Reboul J, Sabatier L, Guichou J, Kohara Y. TLR-independent control of innate immunity in *C. elegans* by the TIR domain adaptor protein TIR-1, an ortholog of human SARM. Nature Immunology. 2004;5(3):488–94.PMID: 15048112

17. Taffoni C, Omi S, Huber C, Mailfert S, Fallet M, Rupprecht J-F, et al. Microtubule plus-end dynamics link wound repair to the innate immune response. Elife. 2020;9:e45047. https://doi.org/10.7554/eLife.45047 PMID: 31995031
18. Zugasti O, Thakur N, Belougne J, Squiban B, Kurz C, Soulé J, et al. A quantitative genome-wide RNAi screen in *C. elegans* for antifungal innate immunity genes. BMC Biology. 2016;14(1):35. PMID: 27129311
19. Lee S, Omi S, Thakur N, Taffoni C, Belougne J, Engelmann I, et al. Modulatory upregulation of an insulin peptide gene by different pathogens in *C. elegans*. Virulence. 2018;9(1):648–58. PMID: 29405821
20. Ziegler K, Kurz C, Cypowyj S, Couillault C, Pophillat M, Pujol N. Antifungal innate immunity in *C. elegans*: PKCdelta links G protein signaling and a conserved p38 MAPK cascade. Cell Host Microbe. 2009;5(4):341–52. PMID: 19380113
21. Doitsidou M, Poole RJ, Sarin S, Bigelow H, Hobert O. *C. elegans* mutant identification with a one-step whole-genome-sequencing and SNP mapping strategy. PLoS One. 2010;5(11):e15435. https://doi.org/10.1371/journal.pone.0015435 PMID: 21079745
22. Labed SA, Omi S, Gut M, Ewbank JJ, Pujol N. The pseudokinase NIPI-4 is a novel regulator of antimicrobial peptide gene expression. PLoS One. 2012;7(3):e33887. https://doi.org/10.1371/journal.pone.0033887 PMID: 22470487
23. Mok D, Sternberg P, Inoue T. Morphologically defined sub-stages of *C. elegans* vulval development in the fourth larval stage. BMC Developmental Biology. 2015;15:26. https://doi.org/10.1186/s12861-015-0040-5 PMID: 26066484
24. Cohen JD, Bermudez JG, Good MC, Sundaram MV. A *C. elegans* Zona Pellucida domain protein functions via its ZPc domain. PLoS Genet. 2020;16(11):e1009188. https://doi.org/10.1371/journal.pgen.1009188 PMID: 33141826
25. Davis P, Zarowiecki M, Arnaboldi V, Becerra A, Cain S, Chan J, et al. WormBase in 2022-data, processes, and tools for analyzing *Caenorhabditis elegans*. Genetics. 2022;220(4):iyac003. https://doi.org/10.1093/genetics/iyac003 PMID: 35134929
26. Thomas PD, Ebert D, Muruganujan A, Mushayahama T, Albou L-P, Mi H. PANTHER: Making genome-scale phylogenetics accessible to all. Protein Sci. 2022;31(1):8–22. https://doi.org/10.1002/pro.4218 PMID: 34717010
27. Jumper J, Evans R, Pritzel A, Green T, Figurnov M, Ronneberger O, et al. Highly accurate protein structure prediction with AlphaFold. Nature. 2021;596(7873):583–9. https://doi.org/10.1038/s41586-021-03819-2 PMID: 34265844
28. Mistry J, Chuguransky S, Williams L, Qureshi M, Salazar G, Sonnhammer E. Pfam: The protein families database in 2021. Nucleic Acids Research. 2021;49(D1):D412-9. https://doi.org/10.1093/nar/gkaa1062 PMID: 33125078
29. Buchan D, Jones D. The PSIPRED Protein Analysis Workbench: 20 years on. Nucleic Acids Research. 2019;47(W1):W402. PMID: 31251384
30. Craig DB, Dombkowski AA. Disulfide by Design 2.0: a web-based tool for disulfide engineering in proteins. BMC Bioinformatics. 2013;14:346. https://doi.org/10.1186/1471-2105-14-346 PMID: 24289175
31. Drozdetskiy A, Cole C, Procter J, Barton G. JPred4: a protein secondary structure prediction server. Nucleic Acids Research. 2015;43(Web Server issue):W389. PMID: 25883141
32. Kussie P, Gorina S, Marechal V, Elenbaas B, Moreau J, Levine A. Structure of the MDM2 oncoprotein bound to the p53 tumor suppressor transactivation domain. Science. 1996;274(5289):948–53. PMID: 8875929
33. Cottee M, Muschalik N, Wong Y, Johnson C, Johnson S, Andreeva A. Crystal structures of the CPAP/STIL complex reveal its role in centriole assembly and human microcephaly. eLife. 2013;2(e01071):. https://doi.org/10.7554/eLife.01071 PMID: 24052813
34. Macias MJ, Wiesner S, Sudol M. WW and SH3 domains, two different scaffolds to recognize proline-rich ligands. FEBS Lett. 2002;513(1):30–7. https://doi.org/10.1016/s0014-5793(01)03290-2 PMID: 11911877
35. Hendriks G, Gaidatzis D, Aeschimann F, Großhans H. Extensive oscillatory gene expression during *C. elegans* larval development. Molecular Cell. 2014;53(3):380–92. PMID: 24440504
36. Kim D, Grün D, van Oudenaarden A. Dampening of expression oscillations by synchronous regulation of a microRNA and its target. Nature Genetics. 2013;45(11):1337–44. PMID: 24036951
37. Meeuse MW, Hauser YP, Morales Moya LJ, Hendriks G-J, Eglinger J, Bogaarts G, et al. Developmental function and state transitions of a gene expression oscillator in *Caenorhabditis elegans*. Mol Syst Biol. 2020;16(7):e9498. https://doi.org/10.15252/msb.20209498 PMID: 32687264

38. Meeuse MWM, Hauser YP, Nahar S, Smith AAT, Braun K, Azzi C, et al. *C. elegans* molting requires rhythmic accumulation of the Grainyhead/LSF transcription factor GRH-1. EMBO J. 2023;42(4):e111895. PMID: 36688410
39. Tsiairis C, Großhans H. Gene expression oscillations in *C. elegans* underlie a new developmental clock. Curr Top Dev Biol. 2021;14419–43. https://doi.org/10.1016/bs.ctdb.2020.11.001 PMID: 33992153
40. Katsanos D, Ferrando-Marco M, Razzaq I, Aughey G, Southall TD, Barkoulas M. Gene expression profiling of epidermal cell types in *C. elegans* using Targeted DamID. Development. 2021;148(17):dev199452. https://doi.org/10.1242/dev.199452 PMID: 34397094
41. Ghaddar A, Armingol E, Huynh C, Gevirtzman L, Lewis NE, Waterston R, et al. Whole-body gene expression atlas of an adult metazoan. Sci Adv. 2023;9(25):eadg0506. https://doi.org/10.1126/sciadv.adg0506 PMID: 37352352
42. Balasubramaniam B, Topalidou I, Kelley M, Meadows SM, Funk O, Ailion M, et al. Effectors of anterior morphogenesis in *C. elegans* embryos. Biol Open. 2023;12(7):bio059982. https://doi.org/10.1242/bio.059982 PMID: 37345480
43. Birnbaum SK, Cohen JD, Belfi A, Murray JI, Adams JRG, Chisholm AD, et al. The proprotein convertase BLI-4 promotes collagen secretion prior to assembly of the *Caenorhabditis elegans* cuticle. PLoS Genet. 2023;19(9):e1010944. https://doi.org/10.1371/journal.pgen.1010944 PMID: 37721936
44. Cohen J, Sundaram M. *C. elegans* apical extracellular matrices shape epithelia. J Dev Biol. 2020;8(4):E23.
45. Vuong-Brender TTK, Suman SK, Labouesse M. The apical ECM preserves embryonic integrity and distributes mechanical stress during morphogenesis. Development. 2017;144(23):4336–49. https://doi.org/10.1242/dev.150383 PMID: 28526752
46. Gerstein MB, Lu ZJ, Van Nostrand EL, Cheng C, Arshinoff BI, Liu T, et al. Integrative analysis of the *Caenorhabditis elegans* genome by the modENCODE project. Science. 2010;330(6012):1775–87. PMID: 21177976
47. Johnson L, Vo A, Clancy J, Myles K, Pooranachithra M, Aguilera J. NHR-23 activity is necessary for *C. elegans* developmental progression and apical extracellular matrix structure and function. Development. 2023;150(10):dev201085. PMID: 37129010
48. Forman-Rubinsky R, Cohen JD, Sundaram MV. Lipocalins Are Required for Apical Extracellular Matrix Organization and Remodeling in *Caenorhabditis elegans*. Genetics. 2017;207(2):625–42. https://doi.org/10.1534/genetics.117.300207 PMID: 28842397
49. Katz SS, Barker TJ, Maul-Newby HM, Sparacio AP, Nguyen KCQ, Maybrun CL, et al. A transient apical extracellular matrix relays cytoskeletal patterns to shape permanent acellular ridges on the surface of adult *C. elegans*. PLoS Genet. 2022;18(8):e1010348. https://doi.org/10.1371/journal.pgen.1010348 PMID: 35960773
50. Miao R, Li M, Zhang Q, Yang C, Wang X. An ECM-to-nucleus signaling pathway activates lysosomes for *C. elegans* larval development. Developmental Cell. 2020;52(1):21-37.e5. PMID: 31735670
51. Chiyoda H, Kume M, Del Castillo CC, Kontani K, Spang A, Katada T, et al. *Caenorhabditis elegans* PTR/PTCHD PTR-18 promotes the clearance of extracellular hedgehog-related protein via endocytosis. PLoS Genet. 2021;17(4):e1009457. https://doi.org/10.1371/journal.pgen.1009457 PMID: 33872306
52. Serra ND, Darwin CB, Sundaram MV. *Caenorhabditis elegans* Hedgehog-related proteins are tissue- and substructure-specific components of the cuticle and precuticle. Genetics. 2024;227(4):iyae081. https://doi.org/10.1093/genetics/iyae081 PMID: 38739761
53. Minevich G, Park DS, Blankenberg D, Poole RJ, Hobert O. CloudMap: A Cloud-Based Pipeline for Analysis of Mutant Genome Sequences. Genetics. 2012;192(4):1249. PMID: 23051646
54. Stiernagle T. Maintenance of *C. elegans*. Wormbook. 2006;1. PMID: 18050451
55. Motohashi K. A simple and efficient seamless DNA cloning method using SLiCE from *Escherichia coli* laboratory strains and its application to SLiP site-directed mutagenesis. BMC Biotechnol. 2015;15:47. https://doi.org/10.1186/s12896-015-0162-8 PMID: 26037246
56. Davis MW, Jorgensen EM. ApE, A Plasmid Editor: A Freely Available DNA Manipulation and Visualization Program. Front Bioinform. 2022;2:818619. https://doi.org/10.3389/fbinf.2022.818619 PMID: 36304290
57. Fire A, Harrison S, Dixon D. A modular set of lacZ fusion vectors for studying gene expression in *Caenorhabditis elegans*. Gene. 1990;93(2):189–98. PMID: 2121610
58. Schwartz ML, Jorgensen EM. SapTrap, a Toolkit for High-Throughput CRISPR/Cas9 Gene Modification in *Caenorhabditis elegans*. Genetics. 2016;202(4):1277–88. https://doi.org/10.1534/genetics.115.184275 PMID: 26837755

59. Dickinson D, Pani A, Heppert J, Higgins C, Goldstein B. Streamlined genome engineering with a self-excising drug selection cassette. Genetics. 2015;200(4):1035–49. PMID: 26044593

60. Aljohani MD, El Mouridi S, Priyadarshini M, Vargas-Velazquez AM, Frøkjær-Jensen C. Engineering rules that minimize germline silencing of transgenes in simple extrachromosomal arrays in *C. elegans*. Nat Commun. 2020;11(1):6300. https://doi.org/10.1038/s41467-020-19898-0 PMID: 33298957

61. El Mouridi S, Peng Y, Frøkjær-Jensen C. Characterizing a strong pan-muscular promoter (P*mlc-1*) as a fluorescent co-injection marker to select for single-copy insertions. MicroPubl Biol. 2020;2020:10.17912/micropub.biology.000302. https://doi.org/10.17912/micropub.biology.000302 PMID: 32908967

62. El Mouridi S, AlHarbi S, Frøkjær-Jensen C. A histamine-gated channel is an efficient negative selection marker for *C. elegans* transgenesis. MicroPubl Biol. 2021;2021:10.17912/micropub.biology.000349. https://doi.org/10.17912/micropub.biology.000349 PMID: 33437931

63. Altschul SF, Gish W, Miller W, Myers EW, Lipman DJ. Basic local alignment search tool. J Mol Biol. 1990;215(3):403–10. https://doi.org/10.1016/S0022-2836(05)80360-2 PMID: 2231712

64. Paysan-Lafosse T, Blum M, Chuguransky S, Grego T, Pinto B, Salazar G. InterPro in 2022. Nucleic Acids Research. 2023;51(D1):D418-27. PMID: 36350672

65. Abramson J, Adler J, Dunger J, Evans R, Green T, Pritzel A, et al. Accurate structure prediction of biomolecular interactions with AlphaFold 3. Nature. 2024;630(8016):493–500. https://doi.org/10.1038/s41586-024-07487-w PMID: 38718835

66. Potter S, Luciani A, Eddy S, Park Y, Lopez R, Finn R. HMMER web server: 2018 update. Nucleic Acids Research. 2018;46(W1):W200-4. PMID: 29905871 https://doi.org/10.1093/nar/gky362

67. Ashkenazy H, Abadi S, Martz E, Chay O, Mayrose I, Pupko T. ConSurf 2016: an improved methodology to estimate and visualize evolutionary conservation in macromolecules. Nucleic Acids Research. 2016;44(Web Server issue):W344. PMID: 27166375

68. Kamath RS, Fraser AG, Dong Y, Poulin G, Durbin R, Gotta M, et al. Systematic functional analysis of the *Caenorhabditis elegans* genome using RNAi. Nature. 2003;421(6920):231–7. https://doi.org/10.1038/nature01278 PMID: 12529635

69. Zhang X, Harding BW, Aggad D, Courtine D, Chen J-X, Pujol N, et al. Antagonistic fungal enterotoxins intersect at multiple levels with host innate immune defences. PLoS Genet. 2021;17(6):e1009600. https://doi.org/10.1371/journal.pgen.1009600 PMID: 34166401

70. Haase R, Royer LA, Steinbach P, Schmidt D, Dibrov A, Schmidt U, et al. CLIJ: GPU-accelerated image processing for everyone. Nat Methods. 2020;17(1):5–6. https://doi.org/10.1038/s41592-019-0650-1 PMID: 31740823

71. Rodriguez-Ramos J, Rico F. Determination of calibration parameters of cantilevers of arbitrary shape by finite element analysis. Review of Scientific Instruments. 2021;92(4):045001. PMID: 34243426